

# Controlled, Defect-Guided, Metal-Nanoparticle Incorporation onto MoS<sub>2</sub> via Chemical and Microwave Routes: Electrical, Thermal, and Structural Properties

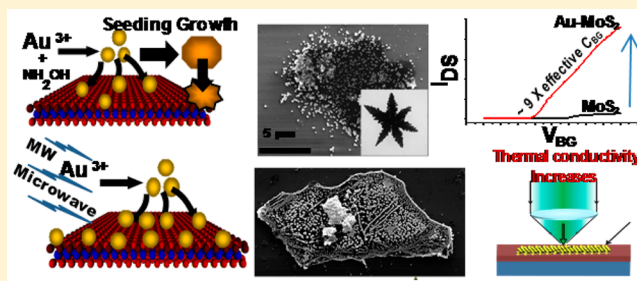
T. S. Sreeprasad,<sup>†</sup> Phong Nguyen,<sup>†</sup> Namhoon Kim, and Vikas Berry\*

Department of Chemical Engineering, Kansas State University, 1005 Durland Hall, Manhattan, Kansas, 66502, United States

**S** Supporting Information

**ABSTRACT:** Ultrathin (0.3–3 nm) metal dichalcogenides exhibit confinement of carriers, evolution of band-structure and photophysical properties with thickness, high on/off rectification (in MoS<sub>2</sub>, WS<sub>2</sub>, and so forth) and high thermal absorption. Here, we leverage the stable sulfur/nobel-metal binding to incorporate highly capacitive gold nanoparticles (Au NPs) onto MoS<sub>2</sub> to raise the effective gate-voltage by an order of magnitude. Functionalization is achieved via both diffusion limited aggregation and instantaneous reaction arresting (using microwaves) with selective deposition on crystallographic edges (with 60° displacement). The electrical, thermal, and Raman studies show a highly capacitive interaction between Au NP and MoS<sub>2</sub> flakes ( $C_{\text{Au-MoS}_2} = 2.17 \mu\text{F}/\text{cm}^2$ ), a low Schottky barrier (14.52 meV), a reduced carrier-transport thermal-barrier (253 to 44.18 meV after Au NP functionalization), and increased thermal conductivity (from 15 to 23 W/mK post NP deposition). The process could be employed to attach electrodes to heterostructures of graphene and MoS<sub>2</sub>, where a gold film could be grown to act as an electron-tunneling gate-electrode connected to MoS<sub>2</sub>.

**KEYWORDS:** Metal dichalcogenides, MoS<sub>2</sub>, graphene, gold nanoparticles, nanotechnology, thermal transport



Elimination of interfacial influences and evolution of confinement by isolating sheets from layered materials has led to the realization of a wide variety of phenomena and extraordinary applications. This outcome was first observed in graphene, where due to the emergent electronic structure with massless Dirac fermions, ballistic carrier transport was achieved.<sup>1</sup> As a semiconducting analog of two-dimensional (2D) graphene, MoS<sub>2</sub> monolayer is a three-atom-thick layered transition-metal dichalcogenide, composed of a stratum of molybdenum atoms sandwiched between two layers of sulfur atoms in a trigonal prismatic (or antiprismatic) lattice. The relatively weak interlayer interaction between the MoS<sub>2</sub> sheets allows their monolayer crystals (thickness 0.65 nm) to be cleaved mechanically and chemically.<sup>2</sup> Further, the electrical and optical properties of MoS<sub>2</sub> change dramatically with number of layers: bulk MoS<sub>2</sub> exhibits an indirect band gap of 1.2 eV, while monolayer MoS<sub>2</sub> has a direct band gap of ~1.8 eV<sup>3</sup> with enhanced photoluminescence.<sup>4</sup> Single layer MoS<sub>2</sub> field effect transistor (FET) exhibits a mobility of 0.5–15 cm<sup>2</sup>/(Vs) with a high on/off current ratio (10<sup>3</sup> to 10<sup>8</sup>).<sup>5</sup> Recent studies show that MoS<sub>2</sub> can be applied effectively in sensing,<sup>6,7</sup> energy harvesting,<sup>8</sup> and photoelectronic application.<sup>9</sup>

To incorporate MoS<sub>2</sub> into rational applications it is imperative to functionalize it with chemical moieties, which can enable its interface with other nano- or micro-systems. Nanointerfacing can provide an avenue for controlling the electrical and thermal properties of MoS<sub>2</sub>, while metal

functionalization can provide contacts for MoS<sub>2</sub>-graphene heterostructure-devices. Other applications that will be impacted include plasmonic devices, catalytic substrates, Raman active surfaces, controlled photoluminescence, and selective sensing. Further, anchoring gold nanoparticles (Au NP) on heterostructures can enhance photophysical properties for improved optoelectronic application.<sup>10</sup> Here, we report solution-based metal functionalization of few layer MoS<sub>2</sub>, the metal-interfacing mechanism and its influence on the electrical, thermal and structural properties of MoS<sub>2</sub>.

Metal nanostructures were incorporated on chemically (liquid-dispersed-phase) and physically (solid-phase) exfoliated MoS<sub>2</sub> crystals (SPI supplies). This was achieved by reduction of metal salt by chemical, microwave, and thermal routes, and establishing sulfur–metal linkage on MoS<sub>2</sub>. The liquid phase exfoliation and dispersal of MoS<sub>2</sub> (10 mg) was carried out in *N*-methyl-pyrrolidinone (NMP, 10 mL in a 20 mL glass container)<sup>2</sup> via 2 h sonication and 10 min centrifugation (5000 rpm). A silica chip (300 nm silica on n-doped silicon substrate) was immersed in this solution for 2 to 24 h at ambient conditions (Figure 1). The chip was then taken out of the solution, washed, and dried in N<sub>2</sub> flow for further

**Received:** June 20, 2013

**Revised:** July 28, 2013

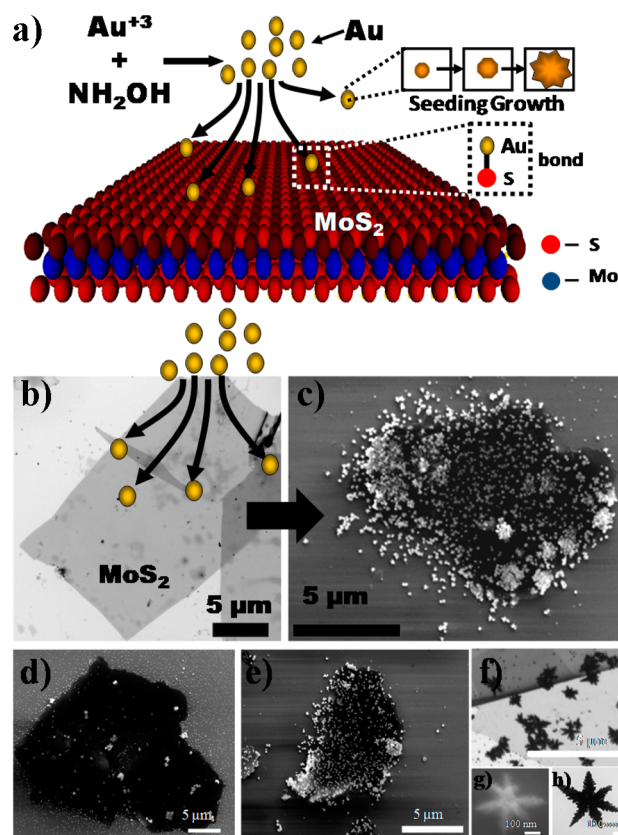


**Figure 1.** (a) Schematic depicting the anchoring of gold nanoparticles on MoS<sub>2</sub> via chemical reduction strategy. (b) TEM image of MoS<sub>2</sub> before functionalization. (c) FESEM image of Au-MoS<sub>2</sub> NP hybrid. (d–f) Time-dependent images of the hybrid at different stages of functionalization. (d,e) FESEM images of the hybrid after 2 and 24 h of reaction respectively. (f) TEM image after 6 h of reaction. (g,h) FESEM and TEM image of the nanoparticle formed on MoS<sub>2</sub> sheet.

characterization. Physically exfoliated MoS<sub>2</sub> sheets were produced via scotch-tape method<sup>5</sup> and transferred onto a silica chip (300 nm silica on n-doped silicon substrate) with (or without) predeposited electrodes (300 nm gold, with 5 μm gap) for electrical studies. The chip was washed with copious amount of water and IPA, dried in N<sub>2</sub> flow for further characterization. Raman spectroscopy and AFM were used to determine the thickness of MoS<sub>2</sub> flakes.

For MoS<sub>2</sub> dispersed in NMP, the metal salt (HAuCl<sub>4</sub> (10 mL, 1 mM) or AgNO<sub>3</sub> (10 mL, 1 mM)) was added and stirred for 5 min. A mild reducing agent, hydroxyl amine (NH<sub>2</sub>OH, 50 wt %, 15 μL) was then added to reduce the metal ions in the solution (10 min). To immobilize the resultant MoS<sub>2</sub>–metal structure, a bare silica chip was introduced into the mixture and kept undisturbed for a set period of time. For functionalization of preimmobilized MoS<sub>2</sub>, the MoS<sub>2</sub>–substrate was immersed in the metal ion solution (10 mL, 1 mM), followed by adding NH<sub>2</sub>OH (50 wt %, 15 μL) and keeping the solution undisturbed for 10 h. The substrate was later removed from the solution and washed thoroughly with water and IPA, dried in N<sub>2</sub> flow, and kept for structural and electrical characterization.

The formation of these nanostructures commence with creation of metal nuclei via nanoscale-crystallization of chemically reduced metal ions. Figure 1a is the mechanistic representation of this functionalization process, where the

hydroxyl amine reduces Au<sup>3+</sup> (Ag<sup>+</sup>) to Au<sup>0</sup> (Ag<sup>0</sup>) (HAuCl<sub>4</sub> + NH<sub>2</sub>OH → Au + 4 HCl + NO). The defects and edges on MoS<sub>2</sub> contain partially unbound sulfur, which binds with Au or Ag and act as sites for metal nuclei seeding and their subsequent growth into bigger nanostructures via Au<sup>0</sup> (Ag<sup>0</sup>) crystal-incorporation. The Au (or Ag) radicals can also incorporate onto the gold nanostructures (GNs) in solution<sup>11,12</sup> and may later anchor onto MoS<sub>2</sub>.<sup>13–15</sup> Further, oxygen can dissociate the Mo–S–Mo bond, resulting in increased defects<sup>16</sup> with reaction time; 2 h (Figure 1d), 6 h (Figure 1f), and 24 h (Figure 1e) of reaction shows increase in the functionalization density with time.

Here, the rate of nucleation,  $J$  (i.e., the number of nuclei formed per unit time per unit volume), can be expressed in the form of the Arrhenius reaction velocity equation<sup>17</sup> ( $J = A \exp[(\Delta E_{\text{des}} - \Delta E_{\text{d}} - \Delta G_{\text{crit}})/(kT)]$ ), where  $\Delta G_{\text{crit}}$  is the critical excess free energy (nucleation),  $\Delta E_{\text{des}}$  is the atomic activation energy of desorption,  $\Delta E_{\text{d}}$  is the surface diffusion activation energy,  $k$  is the Boltzmann constant, and  $T$  is the temperature.<sup>17</sup> These nuclei grow to form highly faceted seed particles. It is known that heterogeneous nucleation (on a suitable surface (like MoS<sub>2</sub>)) occurs with lesser change in free energy compared to the spontaneous nucleation process in supersaturated homogeneous systems.<sup>17</sup> The strong affinity of metal nuclei toward valency-deficient sulfur on MoS<sub>2</sub> surface leads to its anchoring on MoS<sub>2</sub>, which acts as the heterogeneous substrate. Further, these seed-particles moving randomly in solution stick onto MoS<sub>2</sub> with specific lattice facets depending on their chemical potential ( $\nu$ ). Since the sulfur atoms at the edge of the sheets as well as those on surface defects are valency deficient, the gold nuclei get preferentially incorporated during the initial phase of the reaction (Supporting Information Figure S1). The phenomenon is more pronounced in microwave based instantaneous gold nucleation and incorporation process (Figure 2).

Chemically exfoliated,<sup>2</sup> substrate-immobilized MoS<sub>2</sub> sheet (Figure 1b) functionalized with Au NP (Figure 1c, FESEM) show star-shaped GNs (SGNs) and dendritic structures with anisotropically rough arms embedded on the MoS<sub>2</sub> sheet (see Figure 1g,h). The dendritic structure formation involves the surface catalyzed seeded growth of nanoparticles on MoS<sub>2</sub>, which is based on diffusion limited growth.<sup>11</sup> The total rate of formation of GNs ( $r_{\text{F}}$ ) is governed by the rates of diffusion of Au<sup>3+</sup> onto the MoS<sub>2</sub> surface ( $r_{\text{D}}$ ) and the rate of Au incorporation into a growing dendritic structure ( $r_{\text{G}}$ );  $r_{\text{F}}^{-1} = r_{\text{D}}^{-1} + r_{\text{G}}^{-1}$ . Here,  $r_{\text{G}} \gg r_{\text{D}}$ , since metal incorporation is catalytic. Therefore, the dendritic structure is governed by rate of diffusion ( $r_{\text{D}}$ ), which has a strong dependence on temperature. Consistently, our reaction at the room temperature exhibited the SGNs at 4 °C the process yielded comparatively smaller particles with lower density and at higher temperature of 60 °C a larger density of irregular fractal structures of NPs were produced (Supporting Information Figure S2). At lower temperature, the resistance for diffusion ( $k_{\text{D}}^{-1} \propto T^{-1.5}$ ) and particle incorporation ( $k_{\text{G}}^{-1} \propto \exp(E_{\text{A}}/(RT))$ ) increases leading to a smaller particle size and lower density. At room temperature,  $k_{\text{D}}$  ( $< k_{\text{G}}$ ), is believed to increase more than  $k_{\text{G}}$  and will result in the formation of dendritic structures. Moreover, due to the difference in the surface  $\nu$  induced by small deformations, anisotropic growth occurs. As suggested by Mullins-Sekerka instability,<sup>18,19</sup> irregular surfaces with high  $\nu$  grow more preferentially than blunt surfaces with low  $\nu$ . Further, high mass-transfer rates and the chemical



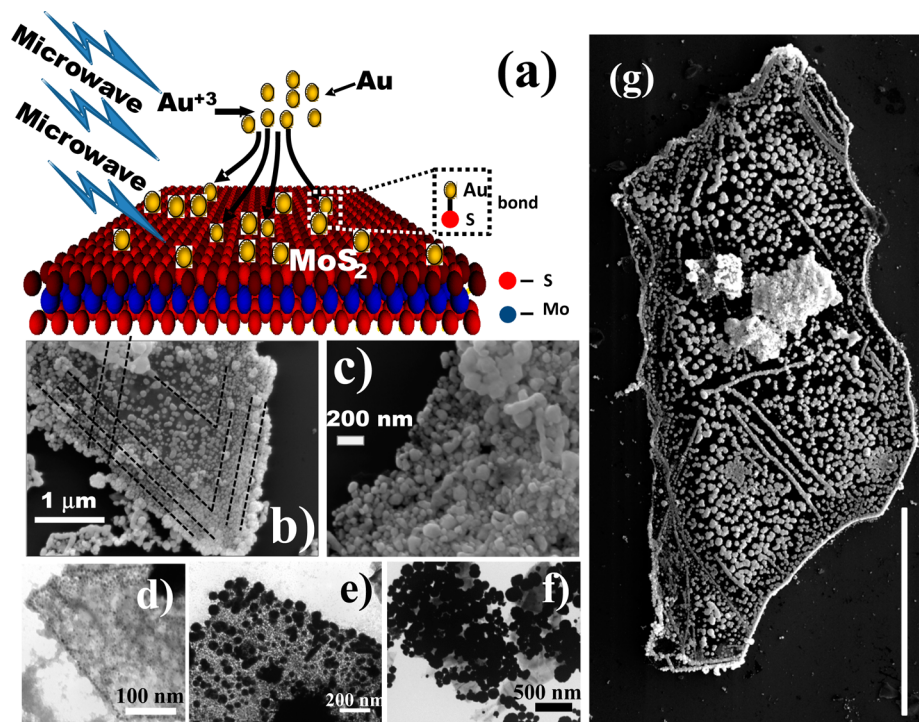


**Figure 2.** (a) Schematic depicting the anchoring of gold nanoparticles on MoS<sub>2</sub> via MW irradiation. (b,c) Large area and higher-magnification FESEM image of Au-MoS<sub>2</sub> NP hybrid. (d–f) FESEM images of the hybrid at different stages/times of functionalization: (d) 2 s, (e) 5 s, and (f) 10 s of MW irradiation. (g) FESEM images showing the preferential edge and/or defect functionalization of gold nanoparticles on turbostatic multilayer MoS<sub>2</sub>. A large number of gold nanoparticles formed in lines indicating the presence of edges or defects. Scale bar 30 μm.

potentials at higher temperatures result in a nanoparticle-cluster formation on MoS<sub>2</sub> surfaces. Since this is diffusion limited process conducted over a large time-scale, the selectivity with respect to edge is low. Micrographs of Ag NPs functionalization can be found in the Supporting Information (Figure S3).

It is important to mention that MoS<sub>2</sub> acts as a stabilizing agent for the GNs, since in the absence of MoS<sub>2</sub> the NPs settle down to the container floor. The formed composite was analyzed using energy dispersive spectroscopy (EDS). The elemental maps and the EDS spectrum validate the formation of proposed hybrid structure (Supporting Information, Figure S4).

Metal NP incorporation onto MoS<sub>2</sub> sheets can also be induced by microwave (MW) aided instantaneous reduction and incorporation (Figure 2a). Here, local dielectric heating from MW exposure (1.05 kW, 2450 MHz) is applied on an aqueous solution of metal salt (0.1 mM) and MoS<sub>2</sub> (solvent assisted exfoliation, 500 μL of parent solution in 10 mL) for 2 to 15 s. The mechanism of attachment is similar to that for chemically reduced Au, where the valency deficient sulfur atoms in the matrix act as nucleating and anchoring sites (Figure 2b, 2c) for Au NP hybrids; however, the process of nucleation, implantation, stabilization on the MoS<sub>2</sub> sheets and nuclei growth is simultaneous and expeditious. This is due to high local temperatures, which eliminates diffusion limited growth and dendritic structure formation, while ensuring that large density of nanoparticles is embedded onto the sheets. Here, microwave induces space-confined heating given by  $E = fe'(\tan \delta)P^2$ , where  $P$  is the microwave power,  $f$  is the frequency of the microwave,  $e'$  is the dielectric constant of the solvent, and  $\delta$  is the loss factor. In high dielectric solvents such as water, the rapid dipolar rotations of the polarized water molecules creates local heating and regions of high kinetic energy. This reduces

the barrier and duration of ion reduction, nucleation, and incorporation, leading to formation of NPs on MoS<sub>2</sub> (note: total time of MW is 2–15 s). Here, reduction and nucleation are independent, while incorporation process is dependent on the interaction between the metal and sulfur, which is higher at the edges even for small duration of MW exposure. It is for this reason that the gold nanoparticle deposition on MoS<sub>2</sub> edges is clearly evident (Figure 2b,g and Supporting Information, Figure S5). This was verified further by using a multilayered MoS<sub>2</sub>, where functionalization occurs preferentially on the edges on the multilayer structures, indicated by the formation of NPs in straight lines (Figure 2b) with angular displacement of 60°, evidence of crystallographic deposition of metal nanostructures. On turbostatic crystals, the angle can be variable; however, the NP deposition on straight lines is still observed (Figure 2g). Consistently, the selectivity of functionalization on the edges is higher at smaller durations of MW irradiation (2 s) (Figure 2d and Supporting Information Figure S5), while the number-density and size of the nanoparticles formed is higher for longer irradiation times (Figure 2 d–f). Further, the density of GNs produced on physically exfoliated MoS<sub>2</sub> (on substrate) was lesser than for solution dispersed MoS<sub>2</sub>. This is attributed to a low degree of surface defects on physically exfoliated MoS<sub>2</sub>. Further, the lack of capping molecule on the anchored gold nanoparticles implies their high catalytic efficiency.<sup>12</sup>

Comparative capacitance studies between gold and MoS<sub>2</sub> (shown later) for our process and the electron microscopy confirms an intimate contact between MoS<sub>2</sub> and Au NP in the hybrid (Figures 1 and 2 and Supporting Information Figure S6). The effect of formation of such a hybrid on the lattice of MoS<sub>2</sub> was analyzed using Raman spectroscopy. The pristine MoS<sub>2</sub> and MoS<sub>2</sub>-gold NP hybrid were analyzed using Raman spectroscopy (Figure 3), which shows the  $E_{2g}^1$  (~391 cm<sup>-1</sup>)

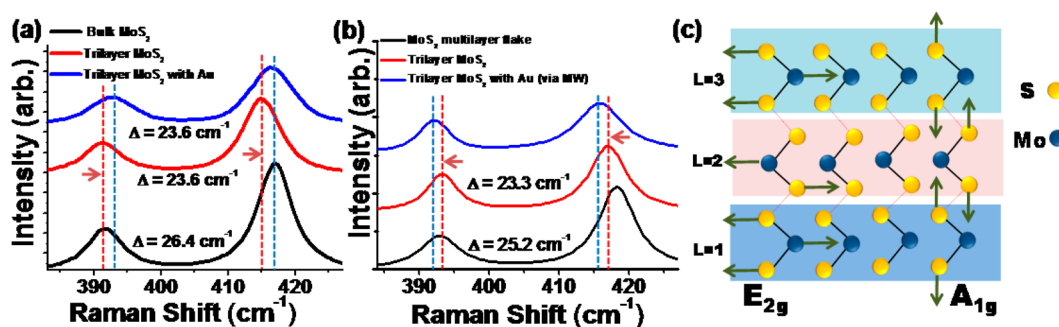


**Figure 3.** Raman spectrum of Au-MoS<sub>2</sub> hybrid prepared via (a) chemical reduction and (b) microwave irradiation. The Raman spectra of the bulk MoS<sub>2</sub> sheet showing the E<sub>2g</sub> (~385 cm<sup>-1</sup>, in plane vibration) and A<sub>1g</sub> (~410 cm<sup>-1</sup>, out of plane vibration) peaks (a). The  $\Delta$  represents the difference between the Raman peak positions (i.e., A<sub>1g</sub> - E<sub>2g</sub>), and is used to determine the number of MoS<sub>2</sub> layers. For  $\Delta \sim 23$  cm<sup>-1</sup>, the number of layers was estimated to be three. After gold deposition, the A<sub>1g</sub> and E<sub>2g</sub> peaks upshift by ~1 cm<sup>-1</sup> (in a), which implied p-doping. In the case of microwave irradiation (b), a downshift of features can be observed, implying n-doping. (c) Illustration of relevant modes of vibration in MoS<sub>2</sub>.

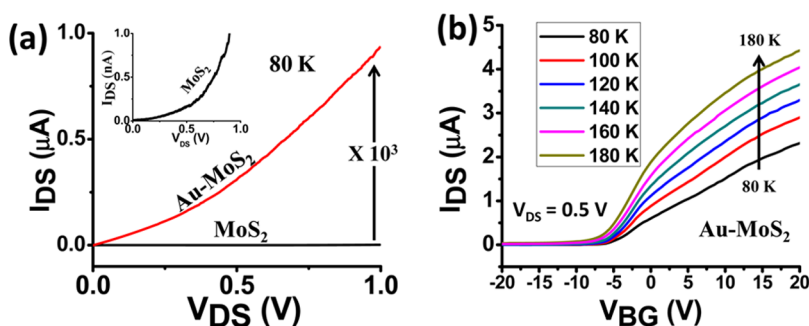


**Figure 4.** (a) At 80 K the conductivity of MoS<sub>2</sub> device is increased 10<sup>3</sup> folds after gold functionalization (Au-MoS<sub>2</sub>). The inset shows an enlarged view of I<sub>DS</sub> versus V<sub>DS</sub> response for MoS<sub>2</sub> at 80 K. (b) The gating characteristic (I<sub>DS</sub> versus V<sub>BG</sub>) for Au-MoS<sub>2</sub> FET between 80 and 180 K with 0.5 V applied bias voltage (V<sub>DS</sub>).

and A<sub>1g</sub> (~417 cm<sup>-1</sup>) peaks corresponding to the in plane (2 S atoms in opposite direction to the Mo atom) and out of plane (S atoms in opposite directions) vibrations for bulk MoS<sub>2</sub> (Figure 4c).<sup>20</sup> The difference in the peak positions,  $\Delta$  (difference between the E<sub>2g</sub> and A<sub>1g</sub> peak positions), is known to be an indicator of the number of layers.<sup>3</sup> Here, when the number of layers increases, the van der Waals force between MoS<sub>2</sub> sheets results in a higher force constant for atomic vibration. This affects the E<sub>2g</sub> peak predominantly and results in its blue shift. On the other hand, stacking-induced long-range Coulombic interlayer interactions result in a redshift of atomic vibrations, predominantly observed in A<sub>1g</sub>. As a combined effect, the energy gap ( $\Delta$ ) between E<sub>2g</sub> and A<sub>1g</sub> decreases with reduction in number of layers.<sup>16,21</sup> Bulk MoS<sub>2</sub> shows a  $\Delta$  value of 26 cm<sup>-1</sup>. Our sample after exfoliation exhibited a  $\Delta$  value 23.6 cm<sup>-1</sup> suggesting that they are trilayer MoS<sub>2</sub> sheets. Further, the line width for our trilayer samples also increased in comparison to the bulk MoS<sub>2</sub>. This is because for bulk MoS<sub>2</sub>, the inner layers dominate the Raman intensity resulting in a reduced line width. Thinning down of MoS<sub>2</sub> and the associated structural changes results in the development of varying force constants between the inner and outer layers of the material inducing an increased line width with decrease in the number of layers (Figure 4).<sup>21</sup>

After attachment of Au nanoparticles via chemical functionalization, the Raman showed a distinct upshift of features indicating p-type doping of MoS<sub>2</sub> sheets,<sup>22</sup> consistent with recent studies (Figure 3a).<sup>23</sup> However, MW assisted functionalization showed a small down-shift of features pointing toward n-type doping. Several experiments confirm this trend and

indicate the importance of the mode of bonding on the polarity of doping. It is important to mention that MW process did not have hydroxylamine and exhibited higher edge-selectivity, which might have a role to play in doping MoS<sub>2</sub>. More studies are required to identify the cause of the difference in doping polarity.

The influence of the metal functionalization (chemical) on the electrical properties of mechanically exfoliated layered-MoS<sub>2</sub> between electrodes (gold, 5 μm channel width) was characterized for the Schottky barrier, Au-MoS<sub>2</sub> capacitance, thermal-barrier, carrier concentration and mobility. Each device was washed in acetone and isopropanol mixture (3:1), dried in N<sub>2</sub> and placed in a cryostat chamber at 10<sup>-4</sup> Torr. The device was thermally annealed at 120 °C, followed by electric Joule heating (2 V, 2 μA) for 3 h to remove adsorbates and to reduce contact resistance between MoS<sub>2</sub> and Au contact.

Because of the mismatched work-function between MoS<sub>2</sub> flakes (~25 nm thick, confirmed by atomic force microscopy (AFM), Supporting Information, Figure S7, 5 μm channel) and metal contacts, a Schottky barrier is introduced at the interface between source/drain electrodes and MoS<sub>2</sub>. Here, as the source-drain bias voltage increases, the carrier hopping through the Schottky barrier increases (see Supporting Information, Figure S8).<sup>24</sup> This phenomenon translates into an increase in current at high source-drain voltage in the I-V curve. Further, at intermediate bias voltage, the total current I is governed by the Schottky barrier according to the following equation:<sup>25,26</sup>  $I = S J_s \exp[V_{DS}(q/(kT) - 1/(E_0))]$ , where J<sub>s</sub> is a slowly varying function of applied bias, S is contact area associated with the Schottky barrier, V<sub>DS</sub> is the source-drain bias voltage, q is

magnitude of electron charge,  $k$  is the Boltzmann constant,  $T$  is the absolute temperature, and  $E_0$  is the Schottky barrier. Here,  $E_0 = E_{00} \coth[(qE_{00})/(kT)]$  with  $E_{00} = [(qh)/(4\pi)][n/(m^*\epsilon_r\epsilon_0)]^{1/2}$ , where  $E_{00}$  is the Padovani-Stratton parameter,  $n$  is carrier concentration of MoS<sub>2</sub> sample,  $m^*$  is effective electron-mass in MoS<sub>2</sub>,  $\epsilon_r$  is the relative permittivity of MoS<sub>2</sub>,  $\epsilon_0$  is the vacuum permittivity, and  $h$  is the Planck's constant. From the logarithmic plot of total current  $I$  versus  $V_{DS}$ , the average Schottky barrier and carrier concentration of MoS<sub>2</sub> sample can be evaluated to be 14.52 meV and  $1.39 \times 10^{15} \text{ cm}^{-3}$ , respectively (see Supporting Information, Figure S9). From the calculated carrier concentration, the average electron mobility is estimated to be  $3.11 \text{ cm}^2\text{V}^{-1}\text{s}^{-1}$  using the equation  $\mu = 1/(nq\rho)$  where  $\rho$  is the resistivity of MoS<sub>2</sub> sample. This mobility value is consistent with previous measurements from other groups.<sup>27</sup> The Schottky-barrier analysis cannot be applied on the Au-MoS<sub>2</sub> device due to the added capacitance between MoS<sub>2</sub> and the Au NP islands (discussed later).

Figure 4a shows the current–voltage ( $I_{DS}$ – $V_{DS}$ ) behavior of a  $5 \mu\text{m}$  channel of MoS<sub>2</sub> flake before and after gold NP deposition. Post Au NP incorporation, the device exhibits 3 orders of magnitude increase in conductivity at 80 K. For long duration of functionalization, the device shows ohmic and high conductivity, attributed to connected gold channels (leakage). From the  $V_{BG}$  versus  $I_{DS}$  at 160 K (Figure 5), we estimate the

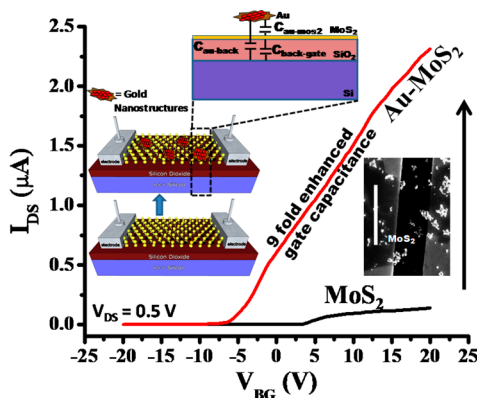


**Figure 5.** Back-gating characteristics (160 K with  $V_{DS} = 0.5 \text{ V}$ ) of MoS<sub>2</sub> and Au-MoS<sub>2</sub> FETs are shown. The top inset shows capacitance circuitry of the Au-MoS<sub>2</sub> device. The on/off ratio of MoS<sub>2</sub> and Au-MoS<sub>2</sub> are  $10^3$  and  $10^2$ , respectively. Bottom-left inset shows the structure of MoS<sub>2</sub> FET with electrical connections used to characterize the device. MoS<sub>2</sub> is deposited on heavily n<sup>+</sup> silicon substrate with 290 nm thick SiO<sub>2</sub>. The substrate acts as a back gate. Au-MoS<sub>2</sub> device shows  $\sim 9$  fold increase in effective gate capacitance. Bottom-right inset shows an FESEM micrograph of gold nanoparticles on MoS<sub>2</sub>. (Bar =  $10 \mu\text{m}$ .)

field-effect mobility of  $\sim 3.71 \text{ cm}^2\text{V}^{-1}\text{s}^{-1}$  for MoS<sub>2</sub> device using the equation:  $\mu = [dI_{DS}/dV_{BG}][L/W][1/(C_{\text{back-gate}}V_{DS})]$  where  $L/W \sim 70$  is the ratio between channel length and width,  $V_{DS}$  is the source-drain voltage, and  $(dI_{DS})/(dV_{BG})$  is the absolute value of the linear slope of the back-gating curve. At a voltage bias of  $V_{DS} = 500 \text{ mV}$ , the current on/off ratio,  $I_{\text{on}}/I_{\text{off}}$  is  $\sim 10^3$  for the  $\pm 20 \text{ V}$  range of  $V_{BG}$  with the off-state current smaller than 100 fA (Figure 5). The subthreshold swing increases from 1.025 to 4.0 V/dec after functionalization in our device (see Supporting Information Figure S10). In contrast to the above results, exposing the MoS<sub>2</sub> device with only water for 24 h without gold source causes a reduction in conductivity ( $\sim 10$

folds) and mobility ( $\sim 2.33$  folds), indicating generation of defects and nucleation sites on MoS<sub>2</sub> via water interaction<sup>28</sup> (see Supporting Information, Figure S11 and S12).

It is known that a top gate electrode (disconnected) along with a bottom gate enhances the net gate capacitance; implying that at lower gate voltage a higher change in source-drain current ( $I_{DS}$ ) can be achieved.<sup>29</sup> We propose that the Au NP deposition on MoS<sub>2</sub> acts as an unconnected top gate with very high capacitance ( $C_{\text{Au-MoS}_2}$ ), which leads to an enhanced effective gate capacitance ( $C_{\text{effective}}$ ), when the back gate is applied ( $C_{\text{back-gate}}$ ). Therefore,  $C_{\text{effective}} = C_{\text{back-gate}} + f(C_{\text{Au-MoS}_2}^{-1} + C_{\text{Au-back}}^{-1})^{-1}$ , where  $C_{\text{Au-back}}$  is the capacitance between gold and silicon and  $f$  is the fraction of MoS<sub>2</sub> area with Au NP. Since  $C_{\text{gold-back}} > C_{\text{gold-MoS}_2} > C_{\text{back-gate}}$ ,  $C_{\text{effective}} \approx fC_{\text{Au-MoS}_2}$ . This implies that the effective capacitance becomes  $C_{\text{Au-MoS}_2}$ , which is higher than the  $C_{\text{back-gate}}$ . For MoS<sub>2</sub> with gold nanostructures acting as gate enhancers, the slope  $(dI_S)/(dV_{BG})$  shows a 9.04 fold increase, implying that effective capacitance increases from  $12 \text{ nF/cm}^2$  ( $= C_{\text{back-gate}}$ ) to  $108.48 \text{ nF/cm}^2$  ( $= C_{\text{effective}} \approx fC_{\text{Au-MoS}_2} = 108.48 \text{ nF/cm}^2$ ) for a Au NP coverage of  $\sim 5\%$ . This implies that the  $C_{\text{gold-MoS}_2} \sim 2.17 \mu\text{F/cm}^2$ , a value similar to the quantum capacitance for graphene.<sup>30–32</sup> This capacitance coupled with gate electrode provides an enhanced pseudomobility<sup>29</sup> of  $33.5 \text{ cm}^2/\text{V}\cdot\text{s}$ . It is important to mention that interfacing MoS<sub>2</sub> with high- $k$  dielectric material can cause dielectric suppression of the Coulomb scattering and modification of the acoustic phonon spectrum.<sup>5,33,34</sup> However, that requires higher (complete) coverage of the dielectric. Further, Fuhrer and Hone<sup>29</sup> showed that capacitive interfacing on relatively thicker dielectric produces a two-orders of magnitude higher pseudomobility than dielectric suppression. Therefore, we conjecture that capacitive coupling is the primary mechanism behind the modified gating behavior of our device.

The polarity of doping induced by metals on MoS<sub>2</sub> strongly depends on the work function ( $\phi$ ) of the metal as well as MoS<sub>2</sub>. MoS<sub>2</sub> work function ( $\phi_{\text{MoS}_2}$ ) is reported to vary from 4.48 to 5.2 eV depending on the layer thickness.<sup>35–38</sup> The same for gold ( $\phi_{\text{Au}}$ ) is reported to be 5.1 eV. Hence, thin flakes of MoS<sub>2</sub> (multilayer) are known to get n-doped<sup>39</sup> when in contact with gold. Interaction of ultrathin MoS<sub>2</sub> (1–3 layers) with the substrate can also modulate the work function. In the present study, anchoring of Au NP on trilayer MoS<sub>2</sub> induces a p-doping as verified by Raman spectroscopy (Figure 3a). This implies that trilayer MoS<sub>2</sub> on silica has work function (and Fermi level position) that allows the electron to flow from MoS<sub>2</sub> to Au, resulting in p-doping. However, our electrical gating measurements show an increase in saturation current after anchoring of Au NPs. The increase in saturation current in n-type MoS<sub>2</sub> implies n-type doping. The difference in polarity between the Raman and electrical measurement is a consequence of two reasons. (1) The MoS<sub>2</sub> sample used for electrical studies are thicker (25 nm, multilayer) compared to the sample used for Raman measurements (trilayer). This in turn translates into a lesser work function. (2) While the sample for Raman measurement was supported on SiO<sub>2</sub>, the electrical measurements were done on SiO<sub>2</sub> chips with predeposited Au electrodes. The interaction of MoS<sub>2</sub> with Au electrodes modulates the Fermi level of MoS<sub>2</sub> (via n-doping<sup>39</sup>) to facilitate the transfer of electron from Au NP to MoS<sub>2</sub> after Au NP deposition. To verify this, Raman spectra was taken from the sample on Au electrode before and after Au NP anchoring. The Raman spectra clearly showed a downshift,



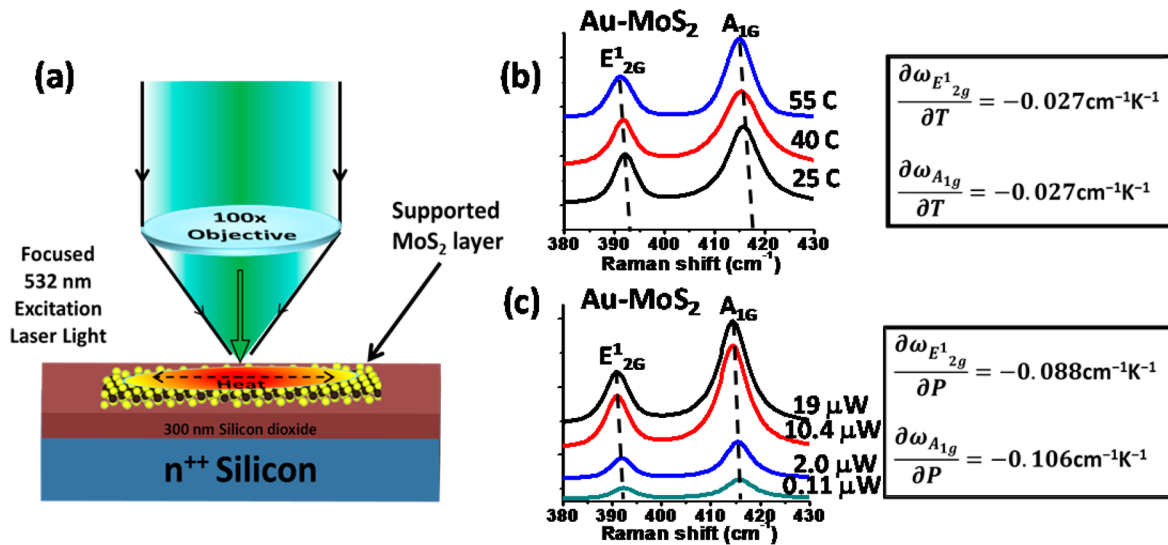


**Figure 6.** (a) Schematic of thermal conductivity experiment showing the 532 nm laser focused on supported MoS<sub>2</sub> sheet. The focus laser generates local hot spot which radially dissipate over MoS<sub>2</sub> sheet. (b) Raman spectra at different temperature and the gradient of E<sub>12g</sub> peaks position with temperature  $[(\delta\omega_{E_{12g}})/(\delta T)]$  for Au-MoS<sub>2</sub> and MoS<sub>2</sub>. (c) Raman spectra at different reflected laser power and the gradient of the E<sub>12g</sub> peaks position with reflected laser power  $[(\delta\omega_{E_{12g}})/(\delta P)]$  for Au-MoS<sub>2</sub> and MoS<sub>2</sub>.

implying n-doping, consistent to the electrical measurement and the theory (Supporting Information, Figure S13).

The strong interaction of chemically deposited Au NP on MoS<sub>2</sub> was compared with sputter deposited Au on MoS<sub>2</sub> by analyzing the respective capacitance between deposited Au and MoS<sub>2</sub>. The capacitance between sputtered gold and MoS<sub>2</sub> was  $\sim 3$  folds less than  $C_{\text{gold-MoS}_2}$  (Supporting Information, Figure S14). This confirms a more intimate contact between MoS<sub>2</sub> and Au deposited via chemical process than physical process, as expected. Moreover, gold-sputtered on MoS<sub>2</sub> exhibits lesser n-doping (see Supporting Information, Figure S14). As mentioned above, the final deposition density of gold NP on MoS<sub>2</sub> is dependent on the defect-density on MoS<sub>2</sub>; however, above about 15% coverage, the gold NPs tends to make conductive channels between the source and drain (Supporting Information Figure S15 and S16).

Variable temperature measurements were carried out to investigate the carrier transport mechanism in the Au-MoS<sub>2</sub> device (Figure 4b). With a decrease in temperature, both Au-MoS<sub>2</sub> and MoS<sub>2</sub> exhibited a decrease in conductivity and an increase in  $V_{\text{DS}}-I_{\text{DS}}$  nonlinearity (Supporting Information, Figure S8). This suggested a finite total thermal barrier for both devices, which can be described as Arrhenius equation  $I_{\text{sat}} = Ce^{(-\phi_{\text{th}}/(k_{\text{B}}T))}$ , where  $I_{\text{sat}}$  is current saturation at  $V_{\text{BG}} = 20$  V (in our experiment),  $C$  is a constant,  $\phi_{\text{th}}$  (eV) is the thermal barrier,  $k_{\text{B}}$  is Boltzmann constant ( $8.617 \times 10^{-5}$  eV K<sup>-1</sup>), and  $T$  (K) is temperature. From the  $\ln(I_{\text{sat}})$  versus  $1/T$  plot, it is observed that Au-MoS<sub>2</sub> and MoS<sub>2</sub> exhibit linear dependence, consistent with the equation. Thermal barrier heights  $\phi_{\text{th}}$  (eV), estimated from the slope of these curve are 253 and 44.18 meV for MoS<sub>2</sub>, and Au-MoS<sub>2</sub> respectively. Furthermore the carrier transport in Au-MoS<sub>2</sub> and MoS<sub>2</sub> can be classified as variable range hopping mechanism due to the linear relationship in  $(\ln I_{\text{DS}} \propto T^{(-1)/3})$  plot (Supporting Information, Figure S17), which involves inelastic tunneling.<sup>11,12,40</sup>

Since the electrical properties of MoS<sub>2</sub> are sensitive to its temperature, it is important to study the heat transport properties in these structures for comprehensive device analysis. This analysis was conducted for both bare and gold

functionalized (via microwave process) trilayer MoS<sub>2</sub> supported on 300 nm SiO<sub>2</sub> (mechanical exfoliation)<sup>21</sup> (schematic shown in Supporting Information, Figure S18). Raman spectroscopy provides an indirect route to measure thermal conductivity of nanomaterials, while its accuracy is dependent on the intensity of the Raman peaks. Lower thickness MoS<sub>2</sub> provides higher Raman signal; therefore, we used trilayer MoS<sub>2</sub> to study its thermal conductivity before and after gold functionalization (a sufficiently large monolayer was not observed even after extensive search). High flux and intensity laser exposure can etch MoS<sub>2</sub> and thus can interfere with the thermal measurements.<sup>41</sup> The maximum laser power used in our measurements was 20  $\mu\text{W}$ , which is 500 times lesser than the power used by Castellanos-Gomez et al.<sup>41</sup> to etch MoS<sub>2</sub>. Control experiment was conducted to study the change in Raman features from exposure to the maximum laser power (20  $\mu\text{W}$ ) for 15 s (Supporting Information Figure S 19). Absence of any noticeable change in Raman peaks indicates that the thermal conductivity measurements are negligibly affected by laser interaction with the samples. Here, a 532 nm laser beam ( $\sim 1$   $\mu\text{m}$  diameter) was focused at the center of trilayer MoS<sub>2</sub> and the generated heat propagates laterally and steadily through the thin layer, presumably due to low thermal conductivity of air (0.025 W/mK) (Figure 6).<sup>21</sup> The intensities of the reflected beam from MoS<sub>2</sub> and from bare silica were measured by a laser power meter to obtain the power absorbed by MoS<sub>2</sub> given by  $P$ . The radial heat conduction through the surface of cross-sectional area  $A$  can be evaluated from the following equation  $\delta Q/\delta t = -k\oint \nabla T \cdot dA$ , where  $Q$  is the amount of heat transferred over time  $t$ ,  $T$  is the absolute equilibrium temperature, and  $k$  is the thermal conductivity. The steady-state, average solution of this equation provides the thermal conductivity:  $k = 1/2\pi d[\delta P/\delta T]$  where,  $d$  is the thickness of MoS<sub>2</sub> layer (2 nm). Here,  $T$  is the equilibrium temperature for a given power,  $P$ . To measure  $k$ , we need  $(\delta P/\delta T)$  or the relationship between power and temperature. This interplay is calculated for MoS<sub>2</sub> indirectly via Raman by correlating the Raman peak position with temperature (controlled externally) and with laser power, then combining them to find  $k$ :  $k = 1/$

$2\pi d(\delta P/\delta T) = 1/2\pi d(\delta\omega/\delta T)(\delta\omega/\delta P)^{-1}$  where,  $(\delta\omega/\delta T)$  is the gradient in the  $A_{1g}$  or  $E_{2g}^1$  Raman peak positions with sample temperature (Supporting Information, Figure S20 and Figure S21), and  $(\delta\omega/\delta P)$  is the gradient in the  $A_{1g}$  or  $E_{2g}^1$  with laser power (Supporting Information, Figure S22 and Figure S23).<sup>42</sup> From these gradients, the thermal conductivity of  $\text{MoS}_2$  and  $\text{Au-MoS}_2$  are evaluated to be 16.2 and 21.3 W/mK respectively (Supporting Information, Table S1 and Table S2). The increase in thermal conductivity is attributed to the high thermal conductivity of gold islands ( $\sim 300$  W/mK), which enhances phonon transport on  $\text{MoS}_2$  platform.

In conclusion, we have shown chemical and MW routes to incorporate Au and Ag nanoparticles on  $\text{MoS}_2$ , which results in significant modulation of its electrical, thermal, and structural properties, and increased effective gate capacitance by 9 folds. Here, a facile sulfur–metal interaction is leveraged to achieve functionalization of metal nanostructures on  $\text{MoS}_2$  via both diffusion limited aggregation and instantaneous reaction arresting. The NP deposition occurs preferentially on the edges and defects and exhibits  $60^\circ$  displacements on certain crystallographic edges. The Raman measurements show that the polarity of doping is dependent on the functionalization route and electrical analysis indicated that the interaction between gold nanoparticles and  $\text{MoS}_2$  flakes is highly capacitive ( $C_{\text{Au-MoS}_2} = 2.17 \mu\text{F}/\text{cm}^2$ ). Through Schottky model analysis, a barrier of 14.52 meV and a mobility of  $3.11 \text{ cm}^2/\text{V}\cdot\text{s}$  (and  $3.71 \text{ cm}^2/\text{V}\cdot\text{s}$  from gating) is evaluated; while the thermal transport barrier reduces from 253 to 44.18 meV after gold nanoparticle functionalization. The thermal conductivity of  $\text{MoS}_2$  was found to increase from 15 to 23 W/mK post nanoparticle deposition. Further, the deposition of highly capacitive gold nanostructures on  $\text{MoS}_2$  can be employed to increase the effective gating by orders of magnitude. Futuristically, this versatile process can provide access to a wide range of functionalized metal dichalcogenides for development of fundamental theories on the optical/Raman<sup>43</sup>/electrical/thermal/structural properties/correlations and novel 2D heterostructures and applications.

## ■ ASSOCIATED CONTENT

### ■ Supporting Information

FESEM images of  $\text{MoS}_2$  flakes at different phases of chemical and microwave functionalization with Au and Ag, EDS spectrum and elemental maps, additional TEM images of  $\text{Au-MoS}_2$  hybrids, AFM image of  $\text{MoS}_2$  device,  $I_{\text{DS}}-V_{\text{DS}}$  curves of  $\text{MoS}_2$  device from 80 to 180 K, Schottky barrier calculation, subthreshold swing, control FET experiments without Au and with Au deposited by sputtering, FESEM images of devices with varying coverage of Au NPs, Raman Spectra of  $\text{Au-MoS}_2$  on silica versus on Au electrodes, conductivity of  $\text{Au-MoS}_2$  with different loading, variable range hopping mechanism, experimental schematic of thermal conductivity measurement via Raman spectroscopy, effect of laser power and exposure time on Raman spectra, linear plot of shift in  $A_{1g}$  and  $E_{2g}^1$  peaks versus temperature and reflected laser power, and thermal conductivity calculation. This material is available free of charge via the Internet at <http://pubs.acs.org>.

## ■ AUTHOR INFORMATION

### Corresponding Author

\*E-mail: [vberry@ksu.edu](mailto:vberry@ksu.edu).

### Author Contributions

<sup>†</sup>T.S.S. and P.N. contributed equally.

## Notes

The authors declare no competing financial interest.

## ■ ACKNOWLEDGMENTS

V.B. thanks the financial support from Terry C. Johnson Center for Basic Cancer Research, and partial support from NSF (CMMI-1054877, CMMI-0939523, and CMMI-1030963) and Office of Naval Research (Grant-N000141110767). V.B. thanks Daming Wei and Dr. James Edgar for their support with the AFM measurement. V.B. thanks Donovan Briggs and Cody Fager for help with exfoliating  $\text{MoS}_2$ .

## ■ REFERENCES

- (1) Novoselov, K. S.; Geim, A. K.; Morozov, S. V.; Jiang, D.; Katsnelson, M. I.; Grigorieva, I. V.; Dubonos, S. V.; Firsov, A. A. Two-dimensional gas of massless Dirac fermions in graphene. *Nature* **2005**, *438* (7065), 197–200.
- (2) Coleman, J. N.; Lotya, M.; O'G'Neill, A.; Bergin, S. D.; King, P. J.; Khan, U.; Young, K.; Gaucher, A.; De, S.; Smith, R. J.; Shvets, I. V.; Arora, S. K.; Stanton, G.; Kim, H. Y.; Lee, K.; Kim, G. T.; Duesberg, G. S.; Hallam, T.; Boland, J. J.; Wang, J. J.; Donegan, J. F.; Grunlan, J. C.; Moriarty, G.; Shmeliov, A.; Nicholls, R. J.; Perkins, J. M.; Grieveson, E. M.; Theuwissen, K.; McComb, D. W.; Nellist, P. D.; Nicolosi, V. Two-Dimensional Nanosheets Produced by Liquid Exfoliation of Layered Materials. *Science* **2011**, *331* (6017), 568–571.
- (3) Mak, K. F.; Lee, C.; Hone, J.; Shan, J.; Heinz, T. F. Atomically Thin  $\text{MoS}_2$ : A New Direct-Gap Semiconductor. *Phys. Rev. Lett.* **2010**, *105* (13), 136805.
- (4) Splendiani, A.; Sun, L.; Zhang, Y.; Li, T.; Kim, J.; Chim, C. Y.; Galli, G.; Wang, F. Emerging Photoluminescence in Monolayer  $\text{MoS}_2$ . *Nano Lett.* **2010**, *10* (4), 1271–1275.
- (5) Radisavljevic, B.; Radenovic, A.; Brivio, J.; Giacometti, V.; Kis, A. Single-layer  $\text{MoS}_2$  transistors. *Nat. Nanotechnol.* **2011**, *6* (3), 147–150.
- (6) Li, H.; Yin, Z.; He, Q.; Li, H.; Huang, X.; Lu, G.; Fam, D. W. H.; Tok, A. I. Y.; Zhang, Q.; Zhang, H. Fabrication of Single- and Multilayer  $\text{MoS}_2$  Film-Based Field-Effect Transistors for Sensing NO at Room Temperature. *Small* **2012**, *8* (1), 63–67.
- (7) Perkins, F. K.; Friedman, A. L.; Cobas, E.; Campbell, P. M.; Jernigan, G. G.; Jonker, B. T. Chemical Vapor Sensing with Monolayer  $\text{MoS}_2$ . *Nano Lett.* **2013**, *13* (2), 668–673.
- (8) Gourmelon, E.; Lignier, O.; Hadouda, H.; Couturier, G.; Bernede, J. C.; Tedd, J.; Pouzet, J.; Salardenne, J. MS<sub>2</sub>(M = W, Mo) photosensitive thin films for solar cells. *Sol. Energy Mater. Sol. Cells* **1997**, *46* (2), 115–121.
- (9) Buscema, M.; Barkelid, M.; Zwiller, V.; van der Zant, H. S. J.; Steele, G. A.; Castellanos-Gomez, A. Large and Tunable Photo-thermoelectric Effect in Single-Layer  $\text{MoS}_2$ . *Nano Lett.* **2013**, *13* (2), 358–363.
- (10) Britnell, L.; Ribeiro, R. M.; Eckmann, A.; Jalil, R.; Belle, B. D.; Mishchenko, A.; Kim, Y. J.; Gorbachev, R. V.; Georgiou, T.; Morozov, S. V.; Grigorenko, A. N.; Geim, A. K.; Casiraghi, C.; Neto, A. H. C.; Novoselov, K. S. Strong Light-Matter Interactions in Heterostructures of Atomically Thin Films. *Science* **2013**, *340* (6138), 1311–1314.
- (11) Jasuja, K.; Berry, V. Implantation and Growth of Dendritic Gold Nanostructures on Graphene Derivatives: Electrical-Property-Tailoring and Raman-Enhancement. *ACS Nano* **2009**, *3* (8), 2358–2366.
- (12) Jasuja, K.; Linn, J.; Melton, S.; Berry, V. Microwave-Reduced Uncapped Metal Nanoparticles on Graphene: Tuning Catalytic, Electrical, and Raman Properties. *J. Phys. Chem. Lett.* **2010**, *1* (12), 1853–1860.
- (13) Lin, J.; Li, H.; Zhang, H.; Chen, W. Plasmonic enhancement of photocurrent in  $\text{MoS}_2$  field-effect-transistor. *Appl. Phys. Lett.* **2013**, *102* (20), 203109–3.
- (14) Govinda Rao, B.; Matte, H. S. S. R.; Rao, C. N. R. Decoration of Few-Layer Graphene-Like  $\text{MoS}_2$  and  $\text{MoSe}_2$  by Noble Metal Nanoparticles. *J. Clust. Sci.* **2012**, *23* (3), 929–937.

- (15) Xinjun Chu; Yao, G.; Andrew Thye Shen, W.; Xue-Sen, W. Size-tunable Au nanoparticles on MoS<sub>2</sub> (0001). *Nanotechnology* **2012**, 23 (37), 375603.
- (16) Li, H.; Zhang, Q.; Yap, C. C. R.; Tay, B. K.; Edwin, T. H. T.; Olivier, A.; Baillargeat, D. From Bulk to Monolayer MoS<sub>2</sub>: Evolution of Raman Scattering. *Adv. Funct. Mater.* **2012**, 22 (7), 1385–1390.
- (17) Zhuo, R. F.; Feng, H. T.; Chen, J. T.; Yan, D.; Feng, J. J.; Li, H. J.; Geng, B. S.; Cheng, S.; Xu, X. Y.; Yan, P. X. Multistep Synthesis, Growth Mechanism, Optical, and Microwave Absorption Properties of ZnO Dendritic Nanostructures. *J. Phys. Chem. C* **2008**, 112 (31), 11767–11775.
- (18) Mullins, W. W.; Sekerka, R. F. Stability of a Planar Interface During Solidification of a Dilute Binary Alloy. *J. Appl. Phys.* **1964**, 35 (2), 444–451.
- (19) Langer, J. S. Instabilities and pattern formation in crystal growth. *Rev. Mod. Phys.* **1980**, 52 (1), 1–28.
- (20) Bertrand, P. A. Surface-phonon dispersion of MoS<sub>2</sub>. *Phys. Rev. B* **1991**, 44 (11), 5745–5749.
- (21) Lee, C.; Yan, H.; Brus, L. E.; Heinz, T. F.; Hone, J.; Ryu, S. Anomalous Lattice Vibrations of Single- and Few-Layer MoS<sub>2</sub>. *ACS Nano* **2010**, 4 (5), 2695–2700.
- (22) Chakraborty, B.; Bera, A.; Muthu, D. V. S.; Bhowmick, S.; Waghmare, U. V.; Sood, A. K. Symmetry-dependent phonon renormalization in monolayer MoS<sub>2</sub> transistor. *Phys. Rev. B* **2012**, 85 (16), 161403.
- (23) Shi, Y.; Huang, J. K.; Jin, L.; Hsu, Y. T.; Yu, S. F.; Li, L. J.; Yang, H. Y. Selective Decoration of Au Nanoparticles on Monolayer MoS<sub>2</sub> Single Crystals. *Sci. Rep.* **2013**, 3, 1839.
- (24) Lee, K.; Kim, H. Y.; Lotya, M.; Coleman, J. N.; Kim, G. T.; Duesberg, G. S. Electrical Characteristics of Molybdenum Disulfide Flakes Produced by Liquid Exfoliation. *Adv. Mater.* **2011**, 23 (36), 4178–4182.
- (25) Zhang, Z.; Yao, K.; Liu, Y.; Jin, C.; Liang, X.; Chen, Q.; Peng, L. M. Quantitative Analysis of Current–Voltage Characteristics of Semiconducting Nanowires: Decoupling of Contact Effects. *Adv. Funct. Mater.* **2007**, 17 (14), 2478–2489.
- (26) Padovani, F. A.; Stratton, R. Field and thermionic-field emission in Schottky barriers. *Solid-State Electron.* **1966**, 9 (7), 695–707.
- (27) Novoselov, K. S.; Jiang, D.; Schedin, F.; Booth, T. J.; Khotkevich, V. V.; Morozov, S. V.; Geim, A. K. Two-dimensional atomic crystals. *Proc. Natl. Acad. Sci. U.S.A.* **2005**, 102 (30), 10451–10453.
- (28) Cannon, P.; Norton, F. J. Reaction between molybdenum disulphide and water. *Nature* **1964**, 203, 750.
- (29) Fuhrer, M. S.; Hone, J. Measurement of mobility in dual-gated MoS<sub>2</sub> transistors. *Nat. Nanotechnol.* **2013**, 8 (3), 146–147.
- (30) Mohanty, N.; Berry, V. Graphene-Based Single-Bacterium Resolution Biodevice and DNA Transistor: Interfacing Graphene Derivatives with Nanoscale and Microscale Biocomponents. *Nano Lett.* **2008**, 8 (12), 4469–4476.
- (31) Nguyen, P.; Berry, V. Graphene Interfaced with Biological Cells: Opportunities and Challenges. *J. Phys. Chem. Lett.* **2012**, 3 (8), 1024–1029.
- (32) Sreepasad, T. S.; Berry, V. How Do the Electrical Properties of Graphene Change with its Functionalization? *Small* **2012**, 9, 341–350.
- (33) Jena, D.; Konar, A. Enhancement of Carrier Mobility in Semiconductor Nanostructures by Dielectric Engineering. *Phys. Rev. Lett.* **2007**, 98 (13), 136805.
- (34) Wang, H.; Yu, L.; Lee, Y. H.; Shi, Y.; Hsu, A.; Chin, M. L.; Li, L. J.; Dubey, M.; Kong, J.; Palacios, T. Integrated Circuits Based on Bilayer MoS<sub>2</sub> Transistors. *Nano Lett.* **2012**, 12 (9), 4674–4680.
- (35) McMenamin, J. C.; Spicer, W. E. Photoemission studies of layered transition-metal dichalcogenides: MoS<sub>2</sub>. *Phys. Rev. B* **1977**, 16 (12), 5474–5487.
- (36) Kamaratos, M.; Papageorgopoulos, C. A. Adsorption studies on Ar<sup>+</sup>-sputtered MoS<sub>2</sub>(0001). *Surf. Sci.* **1986**, 178 (1ΓC63), 865–871.
- (37) McGovern, I. T.; Williams, R. H.; Mee, C. H. B. Electronic properties of cleaved molybdenum disulphide surfaces. *Surf. Sci.* **1974**, 46 (2), 427–440.
- (38) Schlaf, R.; Lang, O.; Pettenkofer, C.; Jaegermann, W. Band lineup of layered semiconductor heterointerfaces prepared by van der Waals epitaxy: Charge transfer correction term for the electron affinity rule. *J. Appl. Phys.* **1999**, 85 (5), 2732–2753.
- (39) Fontana, M.; Deppe, T.; Boyd, A.; Rinzan, M.; Liu, A.; Paranjape, M.; Barbara, P. Electron-hole transport and photovoltaic effect in gated MoS<sub>2</sub> Schottky junctions. *Sci. Rep.* **2013**, 3, 1634.
- (40) Mohanty, N.; Moore, D.; Xu, Z.; Sreepasad, T. S.; Nagaraja, A.; Rodriguez, A. A.; Berry, V. Nanotomy-based production of transferable and dispersible graphene nanostructures of controlled shape and size. *Nature Commun.* **2012**, 3, 844.
- (41) Castellanos-Gomez, A.; Barkelid, M.; Goossens, A. M.; Calado, V. E.; van der Zant, H. S. J.; Steele, G. A. Laser-Thinning of MoS<sub>2</sub>: On Demand Generation of a Single-Layer Semiconductor. *Nano Lett.* **2012**, 12 (6), 3187–3192.
- (42) Balandin, A. A.; Ghosh, S.; Bao, W.; Calizo, I.; Teweldebrhan, D.; Miao, F.; Lau, C. N. Superior Thermal Conductivity of Single-Layer Graphene. *Nano Lett.* **2008**, 8 (3), 902–907.
- (43) Sajanlal, P.; Pradeep, T. Mesoflowers: A new class of highly efficient surface-enhanced Raman active and infrared-absorbing materials. *Nano Res.* **2009**, 2 (4), 306–320.